nature genetics

The ciliopathy-associated CPLANE proteins direct basal body recruitment of intraflagellar transport machinery

Michinori Toriyama[1], Chanjae Lee[1], S Paige Taylor[2–4], Ivan Duran[2–4], Daniel H Cohn[5], Ange-Line Bruel[6], Jacqueline M Tabler[1], Kevin Drew[1], Marcus R Kelly[7], Sukyoung Kim[1], Tae Joo Park[1,26], Daniela A Braun[8,9], Ghislaine Pierquin[10], Armand Biver[11], Kerstin Wagner[12], Anne Malfroot[13–15], Inusha Panigrahi[16], Brunella Franco[17,18], Hadeel Adel Al-lami[19], Yvonne Yeung[19], Yeon Ja Choi[20,21], University of Washington Center for Mendelian Genomics[22], Yannis Duffourd[6], Laurence Faivre[6,23,24], Jean-Baptiste Rivière[6,25], Jiang Chen[20,21], Karen J Liu[19], Edward M Marcotte[1], Friedhelm Hildebrandt[8,9], Christel Thauvin-Robinet[6,25], Deborah Krakow[5], Peter K Jackson[7] & John B Wallingford[1]

Cilia use microtubule-based intraflagellar transport (IFT) to organize intercellular signaling. Ciliopathies are a spectrum of human diseases resulting from defects in cilia structure or function. The mechanisms regulating the assembly of ciliary multiprotein complexes and the transport of these complexes to the base of cilia remain largely unknown. Combining proteomics, *in vivo* imaging and genetic analysis of proteins linked to planar cell polarity (Inturned, Fuzzy and Wdpcp), we identified and characterized a new genetic module, which we term CPLANE (ciliogenesis and planar polarity effector), and an extensive associated protein network. CPLANE proteins physically and functionally interact with the poorly understood ciliopathy-associated protein Jbts17 at basal bodies, where they act to recruit a specific subset of IFT-A proteins. In the absence of CPLANE, defective IFT-A particles enter the axoneme and IFT-B trafficking is severely perturbed. Accordingly, mutation of CPLANE genes elicits specific ciliopathy phenotypes in mouse models and is associated with ciliopathies in human patients.

Ciliopathies are a broad class of human diseases that share an etiology of defective cilia structure or function. These diseases span skeletal anomalies, craniofacial defects, cystic kidneys, blindness, obesity and other presentations, highlighting the wide array of physiological functions that require components of the cilium[1,2].

Like all organelles, cilia are assembled and maintained by multiprotein machines. For example, the BBSome is a large complex involved in the trafficking of ciliary membrane proteins[3], the Nphp and Mks–B9 complexes assemble the ciliary transition zone, which controls access to the cilium[4,5], and dynein arms drive motile ciliary beating[6]. Likewise, the IFT system, which links cargos to microtubule motors for transport into and out of cilia, comprises two multiprotein complexes, IFT-A and IFT-B[7–11]. IFT-A and IFT-B are frequently described as controlling retrograde and anterograde traffic, respectively. However, both anterograde kinesin motors and retrograde dynein motors can physically associate with IFT-A[7,12–14], and recent studies highlight the role of IFT-A in ciliary entry and anterograde traffic[15,16]. IFT-A and IFT-B are each composed of a multiprotein 'core' in addition to more loosely bound 'peripheral' components[15,17–19].

Although recent reports have begun to define the interactions between IFT complexes and their cargoes[20,21], substantial questions remain concerning the mechanisms by which IFT proteins are

[1]Department of Molecular Biosciences, University of Texas at Austin, Austin, Texas, USA. [2]Department of Orthopaedic Surgery, David Geffen School of Medicine, University of California, Los Angeles, Los Angeles, California, USA. [3]Department of Human Genetics, David Geffen School of Medicine, University of California, Los Angeles, Los Angeles, California, USA. [4]Department of Obstetrics and Gynecology, David Geffen School of Medicine, University of California, Los Angeles, Los Angeles, California, USA. [5]Department of Molecular, Cell and Developmental Biology, University of California, Los Angeles, Los Angeles, California, USA. [6]EA4271GAD Genetics of Developmental Anomalies, FHU-TRANSLAD, Medecine Faculty, Burgundy University, Dijon, France. [7]Baxter Laboratory, Department of Microbiology and Immunology, Stanford University School of Medicine, Stanford, California, USA. [8]Howard Hughes Medical Institute, Boston Children's Hospital, Harvard Medical School, Boston, Massachusetts, USA. [9]Department of Medicine, Boston Children's Hospital, Harvard Medical School, Boston, Massachusetts, USA. [10]Clinical Genetics Centre, University Hospital Center, Liège, Belgium. [11]Pediatric Unit, Hospital Center, Luxemburg, Luxembourg. [12]Cardiological Pediatric Unit, Hospital Center, Luxemburg, Luxembourg. [13]Clinic of Pediatric Respiratory Diseases, Universitair Ziekenhuis Brussel, Brussels, Belgium. [14]Infectious Diseases, Travel Clinic, Universitair Ziekenhuis Brussel, Brussels, Belgium. [15]Cystic Fibrosis Clinic, Universitair Ziekenhuis Brussel, Brussels, Belgium. [16]Department of Pediatrics Advanced, Pediatric Centre Pigmer, Chandigarh, India. [17]Division of Pediatrics, Department of Medical Translational Sciences, Federico II University of Naples, Naples, Italy. [18]Telethon Institute of Genetics and Medicine (TIGEM), Naples, Italy. [19]Department of Craniofacial and Stem Cell Biology, Dental Institute, King's College London, London, UK. [20]Department of Pathology, Stony Brook University, Stony Brook, New York, USA. [21]Department of Dermatology, Stony Brook University, Stony Brook, New York, USA. [22]A full list of members is available at http://uwcmg.org/#/. [23]Clinical Genetics Centre, FHU-TRANSLAD, Children Hospital, CHU Dijon, Dijon, France. [24]Eastern Referral Centre for Developmental Anomalies and Malformative Syndromes, FHU-TRANSLAD, Children Hospital, CHU Dijon, Dijon, France. [25]Laboratory of Molecular Genetics, FHU-TRANSLAD, PTB, CHU Dijon, Dijon, France. [26]Present address: UNIST, Ulsan, Korea. Correspondence should be addressed to J.B.W. (wallingford@austin.utexas.edu).

Received 9 November 2015; accepted 1 April 2016; published online 9 May 2016; corrected after print 30 May 2016; doi:10.1038/ng.3558

recruited to the base of cilia and assembled into IFT trains. Indeed, ciliopathies can result from defects in cytosolic factors that facilitate dynein arm or BBSome transport and assembly[22–28], yet little is known about similar factors that may act on IFT. For example, basal bodies in *Ttbk2*-mutant mice fail to recruit certain subunits of the IFT-A and IFT-B complexes, but they also fail to remove CP110, a key initial step for ciliogenesis[29]. Likewise, Ofd1, Cep83 (Ccdc41) and C2cd3 are implicated in recruiting certain IFT-B subunits to the basal body, but the specificity of these proteins for IFT recruitment is hard to discern, as only a small subset of IFT proteins have been examined in mutants and these proteins have pleiotropic roles in ciliogenesis[30–32].

Here we combine proteomics, *in vivo* cell biology, mouse models and human genetics to characterize a new mechanism governing basal body recruitment and assembly of IFT-A. This new regulatory module is formed by specific protein–protein interactions among Inturned (Intu), Fuzzy (Fuz) and Wdpcp, well-conserved proteins that control planar cell polarity (PCP) in *Drosophila melanogaster* and govern ciliogenesis in vertebrates[33–37] (**Fig. 1a**). We term this new module CPLANE, for ciliogenesis and planar polarity effectors. We show that this module also includes the poorly understood ciliopathy-associated protein Jbts17, which we show recruits CPLANE to basal bodies where it acts specifically by recruiting the IFT-A peripheral proteins. In the absence of CPLANE function, the IFT-A core denuded of peripheral components still undergoes normal bidirectional transport, but the movement of IFT-B is severely impaired. Finally, examination of mutant mice and ciliopathy-associated alleles from human patients reinforces the connection between CPLANE proteins, Jbts17 and the IFT-A machinery, demonstrating that CPLANE has a broad and essential role in ciliogenesis and human ciliopathies.

RESULTS

The CPLANE interactome

Intu, Fuz and Wdpcp are deeply conserved and are essential for vertebrate ciliogenesis (**Fig. 1a**)[36,37]. To gain unbiased insights into the molecular functions of these proteins, LAP-tagged versions of each mouse protein were stably expressed in ciliated mouse kidney IMCD3 cells, lysates were prepared and interacting proteins were affinity purified (**Supplementary Fig. 1a**,**b**). In addition, similar experiments were performed using diverse IFT-A and ciliopathy-related proteins as baits. Mass spectroscopy showed enrichment of the bait protein in each pulldown (**Supplementary Fig. 1c**,**d** and **Supplementary Data 1**), and none of the baits were copurified with over 30 unrelated control proteins, although all baits did pull down common contaminants (**Supplementary Fig. 1e**). From this experiment, we identified a set of roughly 250 proteins that were individually pulled down by each of the three CPLANE proteins (**Supplementary Fig. 2a**).

We identified an extensive interaction network for the CPLANE proteins that involved a wide array of protein machines, including dynein subunits, clathrin adaptors and chaperonins, among others (**Fig. 1b**, **Supplementary Fig. 2b–d** and **Supplementary Data 2**). Given that CPLANE proteins are essential for vertebrate ciliogenesis[36,37], we were surprised to find only selective links to known ciliogenesis proteins. No links were found within the combined CPLANE interactome to many major ciliary machines, including the IFT-B complex, the BBSome, the inversin compartment and the transition zone B9 complex. An exception was the IFT-A complex, as, between them, pulldowns for Intu, Fuz and Wdpcp identified all six subunits of this complex (**Fig. 1b** and **Supplementary Figs. 1c** and **2c**), although no IFT-B proteins were found. Moreover, although pulldown of the IFT-A proteins themselves also efficiently returned other IFT-A proteins, pulldowns with six other ciliogenesis-related baits did not (**Supplementary Fig. 1d**). These data suggest that CPLANE may regulate IFT-A function, which we address below.

Most strongly enriched in all CPLANE pulldowns were the CPLANE proteins themselves, with Intu, Fuz and Wdpcp reciprocally copurified in all combinations (**Supplementary Figs. 1c** and **2d**, and **Supplementary Data 1**). By contrast, these three proteins were entirely absent from pulldowns of six additional ciliopathy-related proteins (**Supplementary Fig. 1c**). Interaction among some CPLANE proteins has also been observed in high-throughput screens of human proteins[38,39]. Moreover, the interactions are conserved in *Drosophila*[40], although these proteins have no apparent role in ciliogenesis in that animal. In addition, the Rsg1 GTPase, which we had previously observed as a Fuz interacting protein[38,39,41], was also strongly associated with Intu and Wdpcp (**Supplementary Fig. 1c**).

Finally, among the most strongly enriched proteins in the CPLANE interactomes was the largely uncharacterized ciliopathy-associated protein Jbts17 (also called C5orf42) (**Fig. 1b** and **Supplementary Figs. 1c** and **2c**). This protein is associated with Joubert, Oral–Facial–Digital (OFD) and Meckel–Gruber syndromes[42–45], and one recent paper identifies it as a component of the transition zone[46]. We confirmed interaction between Jbts17 and all three CPLANE

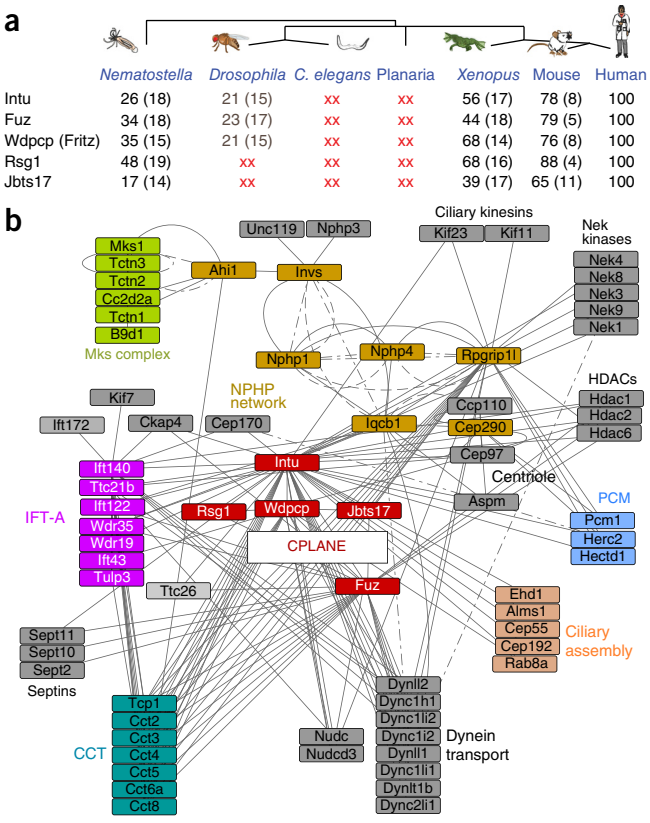

Figure 1 The CPLANE interactome. (**a**) CPLANE proteins are deeply conserved in evolution; numbers indicate percent identity (+ additional percent similarity) to the human protein. "XX" indicates that reciprocal BLAST identified no clear ortholog. (**b**) The extended CPLANE protein network. The results from tandem affinity purification of Intu, Fuz, Wdpcp, IFT-A15 and the published NPHP network[4] were assembled and thresholded for most likely network members; over 2,200 nodes were arranged in Cytoscape (**Supplementary Data 2**), with 78 nodes presented here. Mass spectrometry data will be deposited in ProteomeXchange.

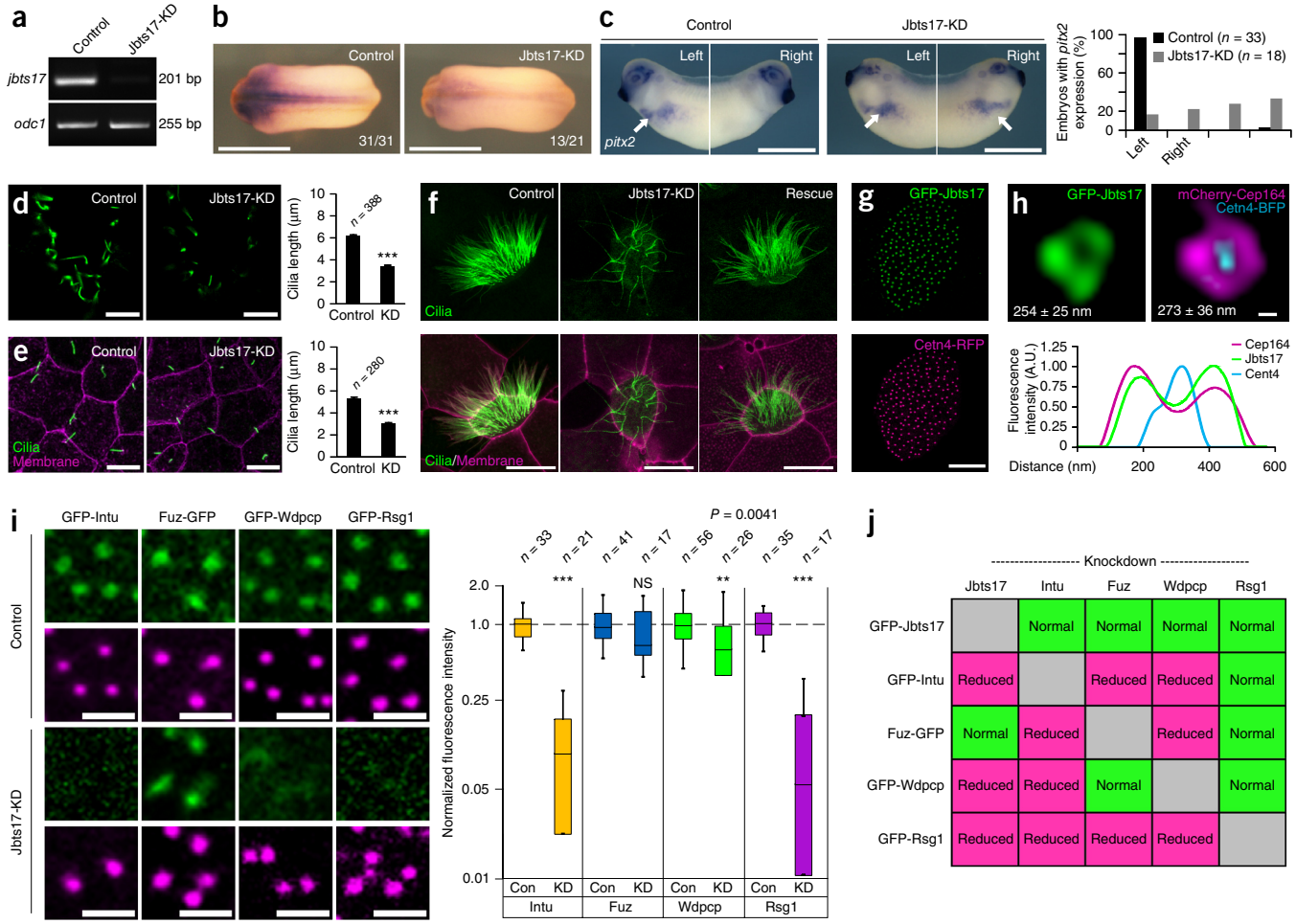

Figure 2 Jbts17 localizes to the base of cilia and is required for ciliogenesis and cilia-mediated patterning. (**a**) RT–PCR demonstrates disrupted *jbts17* splicing after MO injection (Jbts17-KD). *odc1* is the loading control. (**b**) *In situ* hybridization of the Sonic Hedgehog (SHH) direct target *nkx2.2* in control embryos and ones with Jbts17 knockdown (stage 22). Scale bars, 2 mm. Fractions represent the fraction of embryos displaying the phenotype. (**c**) Expression of *pitx2*, which labels the left lateral plate, at stage 26. Arrows indicate signal in left lateral plate mesoderm (LPM); the graph represents *pitx2* expression patterns in embryos. Scale bars, 1 mm. (**d**) Immunostaining for acetylated α-tubulin, which labels cilia, shows ciliogenesis defects after Jbts17 knockdown in the ventral neural tube (stage 22). Scale bars, 10 µm. (**e**) Immunostaining for acetylated α-tubulin shows that Jbts17 knockdown reduces cilia length; cilia numbers are unchanged. Scale bars, 10 µm; membrane-RFP labels membranes. The graphs in **d** and **e** each show pooled data from two independent experiments for cilia length (shown as means ± s.e.m.; $***P < 0.001$). (**f**) MCCs from control embryos, embryos with Jbts17 knockdown showing disrupted cilia, and Jbts17-knockdown embryos rescued with untargeted *jbts17* mRNA labeled by GFP-Cfap20 (green); membrane-RFP labels membranes. Scale bars, 10 µm. (**g**) GFP-tagged Jbts17 localizes near basal bodies (visualized with coexpressed Cetn4-RFP) in an MCC. Scale bar, 10 µm. (**h**) Super-resolution image of GFP-Jbts17 and mCherry-Cep164 at a single basal body; both form rings of ~260 nm in diameter around the basal body, visualized by Cetn4-BFP. Diameters are shown as means ± s.d. in each panel. The graph shows fluorescence intensities (in arbitrary units) for GFP-Jbts17, mCherry-Cep164 and Cetn4-BFP. Scale bar, 100 nm. (**i**) GFP-tagged CPLANE proteins (green) and basal bodies visualized by Cetn4-RFP (magenta) in control and Jbts17-knockdown MCCs. Scale bars, 1 µm. In box plots of CPLANE fluorescence intensities at basal bodies, boxes extend from the 25th to the 75th percentile, with a line at the median; whiskers indicate maximum and minimum values. $**P = 0.0041$, $***P < 0.001$; NS, not significant. Con, control. (**j**) Table summarizing the localization of CPLANE proteins at basal bodies for each knockdown (**Supplementary Fig. 2c–f**).

proteins by coimmunoprecipitation of *in vitro*–translated proteins (**Supplementary Fig. 2e**). Because so little is known about Jbts17, we explored its link to the CPLANE proteins in more detail.

CPLANE protein localization at the base of cilia

Jbts17 is evolutionarily conserved (**Fig. 1a**) and is implicated in varying ciliopathies, but its function remains largely undefined. In *Xenopus laevis*, *jbts17* was expressed in ciliated tissues (data not shown), and knockdown using antisense morpholino oligonucleotides (MOs) to disrupt splicing resulted in ciliopathy-related developmental defects, including failure of neural tube closure, defective Hedgehog signaling and defective left–right patterning (**Fig. 2a–c** and **Supplementary Fig. 3a,b**). Accordingly, ciliogenesis was disrupted in the developing neural tube, in the node and in multiciliated cells (MCCs) (**Fig. 2d–f**). CRISPR-based disruption of *jbts17* also disrupted ciliogenesis, and coinjection with mRNA encoding GFP-Jbts17 rescued both the neural tube and ciliogenesis defects resulting from MO-based knockdown (**Fig. 2f** and **Supplementary Fig. 3a,h**).

Given the physical association of Fuz, Intu and Wdpcp with Jbts17 and Rsg1 (**Supplementary Fig. 1c**), we explored the interrelationships among these proteins in *Xenopus* MCCs, which provide an effective platform for *in vivo* ciliary cell biology. Intu, Fuz, Rsg1 and Jbts17

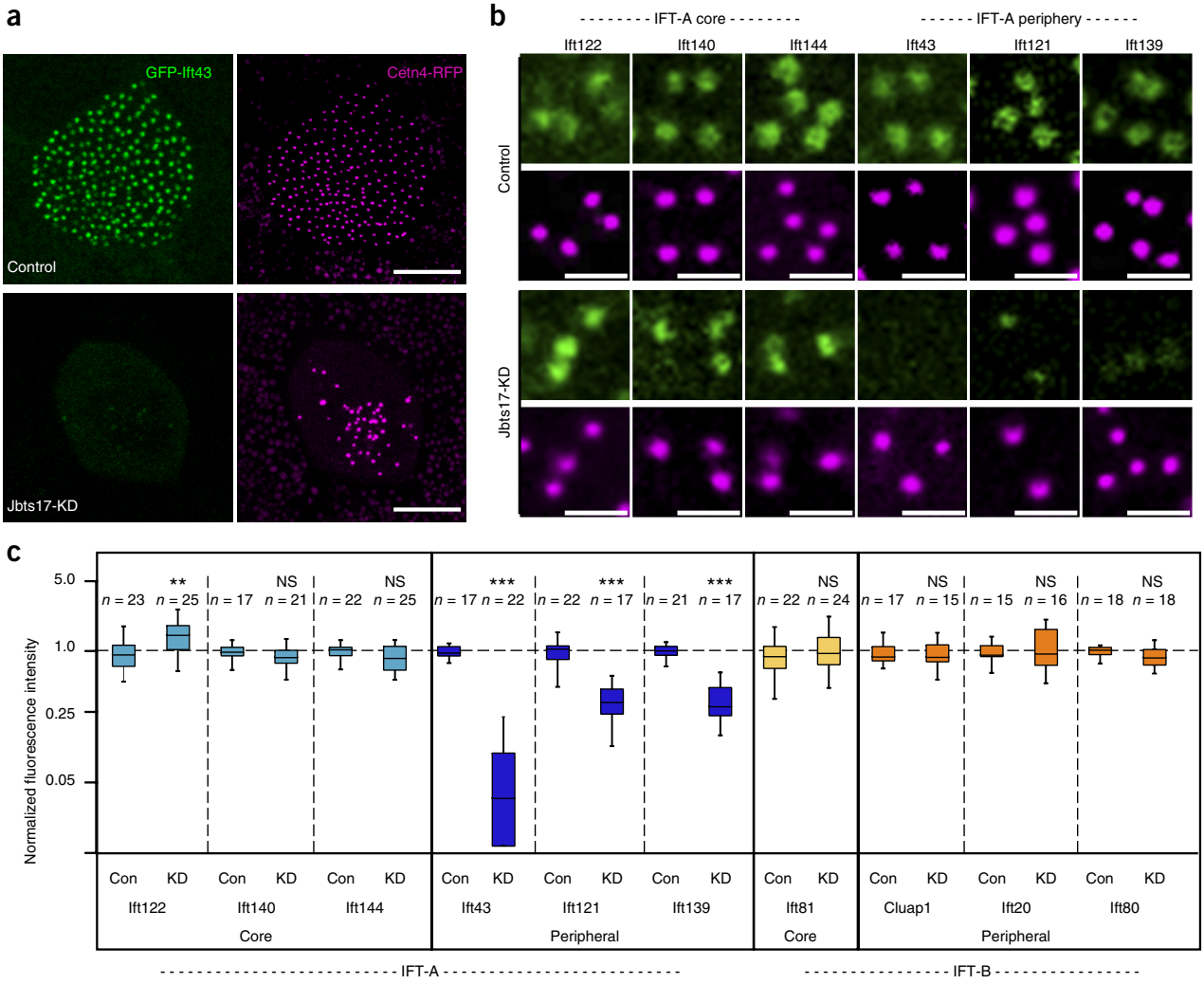

Figure 3 Jbts17 is necessary for recruitment of peripheral IFT-A proteins to basal bodies. (**a**) Ift43 localization at basal bodies in *Xenopus* MCCs, as marked by Cetn4-RFP, is lost in MCCs after Jbts17 knockdown. Scale bars, 10 μm. (**b**) Peripheral IFT-A components are not recruited to Cetn4-RFP-labeled basal bodies after Jbts17 knockdown. IFT-A components are fused to GFP. Scale bars, 1 μm. (**c**) Quantification of IFT protein localization to basal bodies from two independent experiments. Box plots show fluorescence intensities of GFP fusions to indicated IFT proteins normalized against the intensity of Cetn4-RFP (Online Methods). Peripheral IFT-A proteins are specifically lost after Jbts17 knockdown. $^{**}P = 0.0013$, $^{***}P < 0.001$; NS, not significant.

localized robustly around basal bodies but were difficult to detect in axonemes (**Fig. 2g**). Super-resolution imaging showed that GFP-Jbts17 was present in a ring surrounding the basal body, as marked by Centrin 4 (Cetn4)-BFP; this ring was similar to that formed by the distal appendage marker Cep164 (**Fig. 2h**). However, Jbts17 knockdown did not significantly affect recruitment of the distal appendage proteins Cep164 and Ofd1, the transition zone marker Mks1 or the basal body docking protein Hook2 (**Supplementary Fig. 3g**).

To assess the functional relationships of these proteins, we knocked down each CPLANE protein using MOs previously validated by mouse knockout (Online Methods) and then examined basal body localization of the remaining CPLANE components. Our data place Rsg1 at the bottom of the hierarchy: its localization was lost from basal bodies after knockdown of any CPLANE protein, yet its own knockdown did not affect basal body recruitment of any other component (**Fig. 2i,j** and **Supplementary Fig. 3c–f**). Wdpcp and Intu held clear positions upstream of Fuz and Rsg1 but were downstream of Jbts17. Interestingly, Wdpcp and Intu were also each required for the other's basal body localization. The role of Fuz was more complicated: unlike the other CPLANE proteins, Fuz did not require Jbts17 for localization to basal bodies and, although loss of Fuz did disrupt basal body localization of Intu and Rsg1, it did not affect Wdpcp (**Fig. 2i,j**). These data provide an initial framework for the hierarchy of CPLANE protein functions.

A Jbts17 disease variant disrupts Intu localization

JBTS17 (also called *C5orf42*) is mutated in ciliopathies, so we asked whether a disease-causing variant of Jbts17 would disrupt CPLANE function by examining the *Xenopus* cognate of a human Joubert syndrome–associated truncation of Jbts17. The Arg1569* mutant (truncated at the residue equivalent to Arg1602 in humans[45]; **Supplementary Fig. 4a**) failed to localize to basal bodies, whereas another disease-associated truncation mutant (Arg2406*) localized normally, allowing us to map the basal body localization domain of Jbts17 to amino acids 1770–2318 (**Supplementary Fig. 4b**). The pathogenicity of the Arg1569* truncation mutant was apparent: whereas expression of full-length Jbts17 efficiently rescued neural tube defects (NTDs) resulting from Jbts17 knockdown, expression

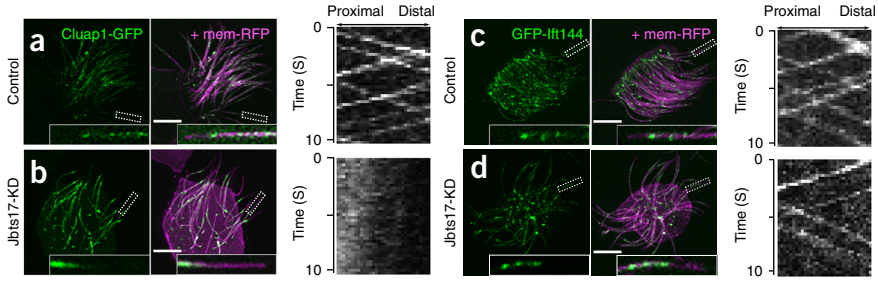

Figure 4 Jbts17 is required for bidirectional axonemal transport of IFT-B particles but not the IFT-A core. (**a**–**d**) Still images from high-speed time-lapse movies of IFT using GFP fusion to IFT proteins (green) and membrane-RFP (magenta). Images are shown for Cluap1-GFP in control (**a**) and Jbts17-morphant (**b**) embryos and for GFP-Ift144 in control (**c**) and Jbts17-morphant (**d**) embryos. Insets show high-magnification views of the localization of IFT particles in a single axoneme in the boxed regions. Scale bars, 10 µm. Associated kymographs representing the movements of IFT particles are shown to the right.

of Jbts17 Arg1569* did not (**Supplementary Fig. 3a**). Linking this embryological defect to cell biological function, Jbts17 Arg1569* also failed to localize to basal bodies (**Supplementary Fig. 4b**), and, unlike wild-type protein, Jbts17 Arg1569* expression could not rescue basal body recruitment of Intu after Jbts17 knockdown (**Supplementary Fig. 4c**). Thus, this Jbts17 disease-associated variant fails to support CPLANE localization and function.

CPLANE recruits peripheral IFT-A proteins to basal bodies

To understand the mechanisms by which CPLANE proteins affect ciliogenesis, we returned to our proteomic data set. We were intrigued by associations between CPLANE proteins and the IFT machinery (**Fig. 1b**) because, although we previously implicated Fuz and Rsg1 in IFT[47,48], their mechanism of action remained ill defined. CPLANE proteins did not interact with IFT-B components but rather specifically interacted with both the IFT-A core and peripheral IFT-A subunits (**Fig. 1b** and **Supplementary Fig. 1c**). Nothing is known about the regulation of peripheral subunit interaction with the IFT-A core, but we reasoned that, by interacting with both, CPLANE could facilitate IFT-A function. Because CPLANE localizes to basal bodies, we tested this notion by assessing basal body recruitment of all six IFT-A proteins after CPLANE disruption.

Strikingly, Jbts17 knockdown specifically disrupted recruitment of the peripheral IFT-A subunits to the basal body. The levels of Ift139, Ift121 and Ift43 at basal bodies were dramatically reduced after Jbts17 knockdown, although recruitment of the three IFT-A core proteins Ift140, Ift144 and Ift122 was not disrupted (**Fig. 3** and **Supplementary Fig. 5a**). In fact, recruitment of Ift122 was consistently increased (**Fig. 3b**,**c**). Although IFT-B is also composed of core and peripheral components, Jbts17 knockdown did not disrupt recruitment of either the peripheral IFT-B proteins Ift20, Ift80 and Cluap1 or the core IFT-B protein Ift81 (**Fig. 3c** and **Supplementary Fig. 5b**). Finally, the link between Jbts17 and IFT-A is likely relevant to disease pathology because, whereas expression of full-length Jbts17 rescued the loss of IFT-A basal body recruitment after Jbts17 knockdown, expression of the Joubert syndrome–associated Jbts17 Arg1569* truncation mutant did not (**Supplementary Fig. 4d**).

Defective IFT-B trafficking in the absence of CPLANE

IFT particles exchange rapidly between axonemes and a cytoplasmic pool around the basal body, so we were curious to know what effect failure to recruit peripheral IFT-A proteins to basal bodies after CPLANE loss would have on IFT trafficking in the axoneme. We used high-speed confocal imaging to assess IFT in MCCs and found that disruption of either Jbts17 or Wdpcp disrupted IFT-B movement, as we previously found with disruption of Fuz[47]. Kymography showed that both peripheral and core components of IFT-B formed stationary accumulations (**Fig. 4a**,**b** and **Supplementary Fig. 5f**), and quantitative microscopy confirmed a significant enrichment of total IFT-B levels in the axoneme ($P = 0.0003$; **Supplementary Fig. 5h**).

These accumulations are reminiscent of the effect of genetic disruption of IFT-A[9,10]. However, the mechanisms by which peripheral IFT-A proteins affect the movement of the IFT-A core have not been examined in detail, and, overall, very little is known yet about the dynamics of IFT-A in vertebrates. We therefore also examined the effect of CPLANE loss on the dynamics of IFT-A peripheral and core proteins in the axoneme. We found that peripheral IFT-A proteins that were not recruited to basal bodies were likewise absent from axonemes after Jbts17 knockdown, consistent with a role for CPLANE in assembly of peripheral subunits onto the IFT-A core (**Supplementary Fig. 5e**).

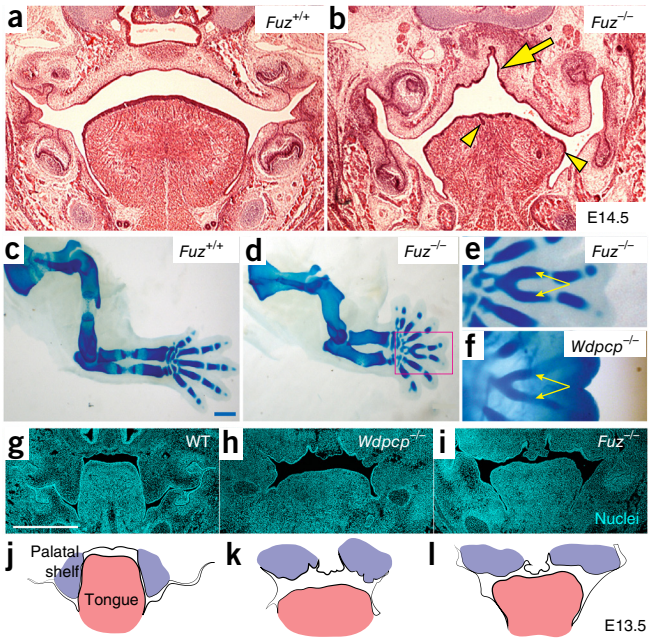

Figure 5 CPLANE-mutant mice display diagnostic features of human OFD6. (**a**,**b**) Frontal sections from wild-type (**a**) and *Fuz*-null (**b**) mice at embryonic day (E) 14.5 show that *Fuz*-mutant mice have high arched palate (arrow) and lobulation of the tongue (arrowheads). Sections were stained with hematoxylin and eosin. (**c**–**e**) Alcian blue staining of E14.5 limbs. *Fuz*-null mice develop polydactyly (the red box in **d** indicates the view shown in **e**). Yellow arrows indicates Y-shaped metacarpals. (**f**) *Wdpcp*-mutant mice develop polydactyly with Y-shaped metacarpals. (**g**–**i**) Frontal sections of E13.5 wild-type (WT) mice (**g**) and *Wdpcp*-mutant (**h**) and *Fuz*-mutant (**i**) embryos. DAPI labels nuclei (cyan). (**j**–**l**) Illustrations highlighting the corresponding palatal condensations (purple) and tongue (pink) in **g**–**i**. Mutant palatal condensations form more medially than do controls and fail to extend into the mouth (see also ref. 50).

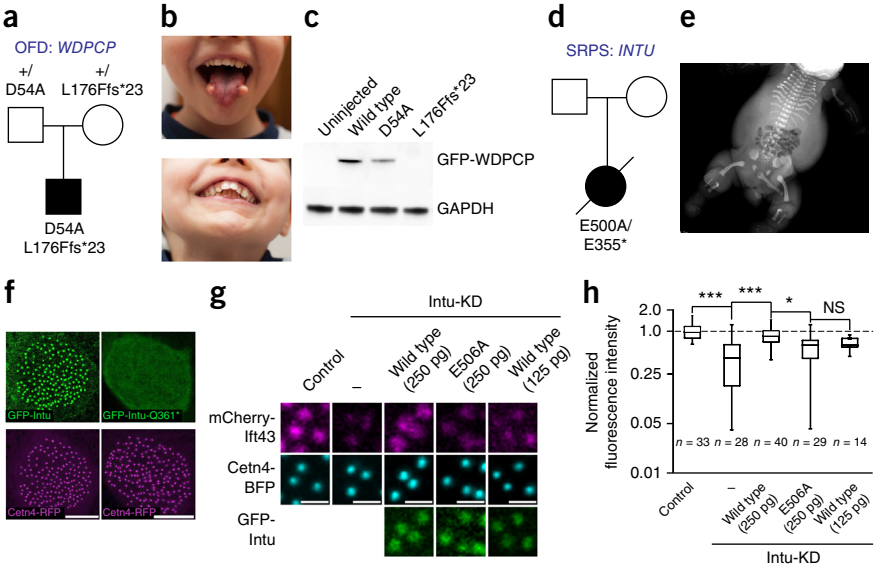

Figure 6 CPLANE gene mutations in human ciliopathies. (**a**) Pedigree showing *WDPCP* mutations in a patient with OFD. (**b**) The patient displays tongue hamartomas and dental anomalies. (**c**) When expressed in *Xenopus* embryos, the allele of human *WDPCP* encoding Asp54Ala produces less protein than the wild-type allele; the allele encoding Leu176Phefs*23 produces no protein. (**d**) Pedigree showing *INTU* mutations in an individual with SRPS. (**e**) X-ray of the affected individual. (**f**) Wild-type *Xenopus* Intu localizes to basal bodies, but the Xenopus cognate of human INTU Glu355* (Gln361*) fails to localize to basal bodies. Scale bars, 10 µm. (**g**,**h**) Expression of *Xenopus* Intu rescues Ift43 localization to basal bodies after Intu knockdown, but the *Xenopus* cognate of human INTU Glu550Ala (*Xenopus* Intu Glu506Ala; see **Supplementary Fig. 6f**) does not. Scale bars, 1 µm. Data shown in **h** are pooled from three independent experiments. $*P < 0.05$, $***P < 0.001$; NS, not significant.

By contrast, IFT-A core proteins were not only present in axonemes at normal levels after Jbts17 knockdown (**Supplementary Fig. 5d**,**h**), but they also underwent bidirectional transport (**Fig. 4c**,**d** and **Supplementary Fig. 5g**), suggesting that the core was intact and could associate with both anterograde and retrograde motors. Similar effects on IFT-A and IFT-B were observed after Wdpcp knockdown (**Supplementary Fig. 5f**,**g**). These data suggest that CPLANE acts by recruiting peripheral IFT-A proteins to the basal body for assembly onto the IFT-A core.

OFD syndrome phenotypes in mouse CPLANE mutants

Together with our proteomic data from mammalian cultured cells, the *in vivo* imaging data from *Xenopus* suggest that Intu, Fuz and Wdpcp are intimately associated with Jbts17, which is encoded by the major gene mutated in human OFD syndrome type 6 (OFD6)[43]. Key diagnostic features of OFD6 include high arched palate, tongue hamartoma and polydactyly characterized by Y-shaped metacarpals[49]. Examining these same features in *Fuz*-null mice, we consistently observed high arched palates, lobulated tongues and Y-shaped metacarpals (**Fig. 5a**–**e**,**g**,**i**,**j**,**l**) (see also ref. 50). We also observed Y-shaped metacarpals and defects in tongue and palate morphology in *Wdpcp* mutants (**Fig. 5f**,**h**,**k**). These genetic data linking CPLANE components to developmental defects characteristic of OFD are consistent with our proteomic link between CPLANE and Jbts17.

Human CPLANE genes are mutated in diverse ciliopathies

Our data argue for a functional and physical association of CPLANE proteins with Jbts17, on the one hand, and with retrograde IFT machinery, on the other hand. We therefore examined CPLANE gene sequences in the exomes of human patients with ciliopathies, focusing on OFD for its connection to Jbts17 (ref. 43) and on short-rib polydactyly syndrome (SRPS) for its association with IFT-A[51,52].

OFD VI, for which *JBTS17* is the major gene[43], has substantial phenotypic overlap with OFD II, including high arched palate, tongue hamartomas and Y-shaped metacarpals[53,54]. Consistent with our data above, exome sequencing of patients with OFD demonstrating these characteristics identified disease-associated mutations in both *WDPCP* and *INTU*. In one patient, a 5-year-old male presenting with facial dysmorphism, tongue hamartoma, high arched palate, tooth abnormalities and postaxial polydactyly, we found transheterozygous mutations in *WDPCP*. One mutation was a frameshift (c.526_527delTT; p.Leu176Ilefs*21), and the other was a missense mutation (c.160G>A; p.Asp54Asn) predicted to alter splicing by Human Splice Finder and ASSP (**Fig. 6a**,**b** and **Supplementary Table 1**). Sanger sequencing confirmed the variants and compound heterozygosity for *WDPCP* by parental segregation (**Fig. 6a**). The altered aspartic acid residue (Asp54) of WDPCP is highly conserved (**Supplementary Fig. 6a**) and has been associated with atypical OFD in one previous patient[55], but no disease-associated alleles of *WDPCP* have yet been tested functionally. We therefore expressed these proteins in *Xenopus* MCCs and found that the frameshift allele resulted in total loss of protein, whereas the point mutation led to a consistent but more modest defect in protein stability (**Fig. 6c**).

We also examined a 10-year-old male presenting with facial dysmorphisms, tongue nodular tags, high arched palate and bilateral central Y-shaped metacarpals (**Supplementary Fig. 6b** and **Supplementary Table 1**). Exome sequencing identified a homozygous frameshift mutation (c.396delT; p.Asn132Lysfs*11) in the *INTU* gene, and Sanger sequencing confirmed that the homozygous *INTU* variant segregated with the phenotype (**Supplementary Fig. 6c**). Brain magnetic resonance imaging (MRI) for both patients with OFD showed no cerebellar abnormality, but cardiac ultrasound showed aortic coarctation and tetralogy of Fallot in the patients with OFD harboring CPLANE gene mutations (**Supplementary Table 1**), consistent with recent data implicating CPLANE genes in cardiac malformation[56].

In addition, we identified a homozygous missense mutation (encoding p.Ala452Thr) in *INTU* in a child with nephronophthisis and growth retardation. The boy, who presented with end-stage renal failure at 10 years of age, was the only affected child of three in a consanguineous family (**Supplementary Table 1**). The identified allele segregated with affected status, and homozygosity mapping showed that the genomic locus of *INTU* was located within a stretch of homozygosity on chromosome 4 (**Supplementary Fig. 6d** and data not shown). This change affects a relatively poorly conserved residue (**Supplementary Fig. 6e**), suggesting that it may be a hypomorphic allele. We also identified a heterozygous mutation (encoding p.Glu365Gly) in *WDPCP* in a boy with cerebellar vermis hypoplasia, ataxia and retinal dystrophy (**Supplementary Table 1**), which may be a modifying allele contributing to this ciliopathy.

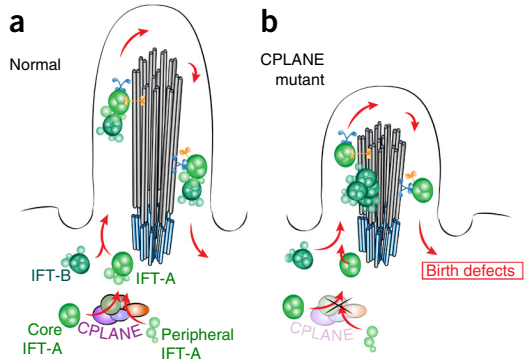

Figure 7 Models for CPLANE function and structure. (**a**) Schematic of normal IFT. Peripheral proteins are assembled onto the IFT-A core in the cytoplasm, and the resulting particles are injected together with IFT-B for bidirectional transport in axonemes. (**b**) In the absence of CPLANE, IFT-A core particles lacking peripheral proteins are injected into axonemes and traffic normally; IFT-B enters axonemes but fails to move in the retrograde direction and accumulates.

Finally, we examined the exomes of individuals with SRPS and identified an affected individual with compound heterozygosity for two *INTU* mutations confirmed by Sanger sequencing (c.1063G>T; p.Glu355* and c.1499A>C; p.Glu500Ala) (**Fig. 6d**,**e** and **Supplementary Fig. 6f**). The affected individual was born preterm at 30 weeks with multiple congenital anomalies, including wide-open fontanel, microphthalmia, tongue hamartomas and tetralogy of Fallot (**Supplementary Table 2**). Radiographic analyses showed multiple skeletal anomalies, including short horizontal ribs, shortened long bones with smooth edges, and pre- and postaxial polydactyly (**Fig. 6e** and **Supplementary Table 2**). To confirm that the identified alleles caused the patient's disease, we examined the function of the INTU mutants. The Glu355* variant failed to localize to basal bodies when expressed in *Xenopus* MCCs (**Fig. 6f**), and, although the p.Glu500Ala alteration did not affect basal body localization, it did significantly impair the ability of the protein to recruit Ift43 (**Fig. 6g**,**h**).

Another case presented with strikingly similar SRPS features (**Supplementary Fig. 6g**,**h** and **Supplementary Table 2**), and a single truncating mutation in *INTU* was confirmed by Sanger sequencing (c.826C>T; p.Gln276*). This change was inherited from the unaffected mother (**Supplementary Fig. 6i**), but, despite extensive analysis, no other changes were found in *INTU*. We examined over 500 changes in the patient's genome that segregated with the disease phenotype, finding only a single change in a gene previously associated with SRPS, a heterozygous change in *WDR35* (encoding IFT121). This change (c.932G>T; p.Trp311Leu) was confirmed by Sanger sequencing and was inherited from the unaffected father (**Supplementary Fig. 6i**); the affected residue is invariant in vertebrates (**Supplementary Fig. 6j**). The clinical presentation of this patient was remarkably similar to that of the individual with compound heterozygosity for *INTU* mutations (**Supplementary Table 2**). The most striking similarity was the distinct polydactyly: whereas most patients with SRPS have 6 or 7 fingers and toes, these two patients both had 9 or 10. Thus, although we cannot rule out a role for mutations in unknown ciliopathy-related genes, the known role for *WDR35* in SRPS, our finding of a role for *INTU* in SRPS, and our finding of physical and functional interactions between IFT-A and CPLANE lead us to suggest that SRPS in this patient results from digenic inheritance of mutations in *WDR35* and *INTU*.

DISCUSSION

Here we characterize an essential but poorly understood protein module, which we term CPLANE (ciliogenesis and planar polarity effector). The CPLANE proteins Intu, Fuz and Wdpcp (Fritz) are deeply conserved in animal evolution (**Fig. 1a**) and were first identified as PCP proteins in *Drosophila*[33–37,40]. In vertebrates, mutation of these genes causes ciliogenesis defects, and, although their role in PCP remains murky, recent reports do suggest that Wdpcp and Intu may govern the localization of core PCP proteins[57–59]. Here we combined proteomics in mammalian cell culture, *in vivo* cell biology in *Xenopus*, and genetic analysis in both mice and humans to demonstrate that CPLANE is an important physical and functional unit governing a specific facet of ciliogenesis, namely the recruitment of IFT-A proteins to the base of cilia and the insertion of complete IFT-A particles into the axoneme (**Fig. 7a**,**b**).

Guided by our proteomic screen, imaging experiments here showed that, in the absence of CPLANE, peripheral IFT-A proteins fail to localize to basal bodies and do not assemble onto the IFT-A core. This connection between CPLANE and IFT-A is strengthened by genetic data linking CPLANE proteins to SRPS, which is generally associated with defects in IFT-A[51,52]. CPLANE does not traffic along axonemes, arguing that it is not a component of the IFT particle itself, a result supported by the fact that CPLANE proteins associate relatively strongly with one another in our proteomic data but comparatively weakly with IFT proteins (**Supplementary Fig. 1c**). Together, these data argue that CPLANE facilitates IFT-A recruitment and assembly at basal bodies, although the precise mechanisms by which it acts remain to be determined.

One possibility is that CPLANE may direct cytoplasmic transport of IFT-A proteins to the base of cilia. This idea is supported by the many links to cytoplasmic dynein machinery in our proteomics data (**Fig. 1** and **Supplementary Fig. 2**). A second line of evidence comes from computational modeling of protein structures (Online Methods), which suggests that CPLANE proteins contain structural domains common in vesicle trafficking machinery (**Supplementary Fig. 7**). Fuz contains a longin domain, and Intu is predicted to fold into a Sec23/Sec24 domain. Likewise, Wdpcp is predicted to form an α solenoid attached to a β propeller, a configuration present in coat proteins, as well as IFT and BBSome subunits[60]. Finally, Jbts17 is an enormous protein (3,167 amino acids) and can be threaded onto multiple protein models, including a Sec23/Sec24 fold, a β-propeller fold and an importin domain.

Another possibility is that the CPLANE proteins may instead influence IFT-A at the level of protein stability and assembly. This possibility is supported by our proteomic data linking Intu, Fuz and Wdpcp individually to all eight subunits of the CCT chaperone complex (**Fig. 1b** and **Supplementary Data 1**). This latter mechanism would be particularly intriguing because similar mechanisms have been proposed linking protein folding to assembly of dynein arms[22,23] and the BBSome[27,28]. Notably, as is true for the CPLANE proteins, disruption of cytosolic assembly factors for dynein arms and the BBSome also cause ciliopathies. This latter possibility is especially exciting because, despite this long history of study, cytosolic factors facilitating basal body recruitment and assembly of IFT particles have not been described.

We also found that peripheral IFT-A proteins were not present in axonemes after CPLANE knockdown, although IFT-A core proteins entered axonemes and trafficked bidirectionally. Because we also observed accumulations of IFT-B in axonemes similar to those found following direct disruption of IFT-A[9–11], our data argue that the peripheral components of IFT-A are essential for association of

IFT-B with IFT-A, at least during retrograde transport (**Fig. 7a**,**b**). This role for the peripheral IFT-A proteins raises interesting questions concerning the mechanism of IFT-B anterograde transport because biochemical data suggest that heterotrimeric kinesin also associates with IFT particles via the IFT-A complex[7,13]. Given that IFT-B moves into axonemes and accumulates there after CPLANE knockdown (**Supplementary Fig. 5c**), it may be that the role for IFT-A peripheral proteins in linking IFT-A to IFT-B is specific to retrograde transport, consistent with the known remodeling of IFT particles upon turnaround[11,12]. Alternatively, homodimeric kinesin 2 associates directly with IFT-B in *Caenorhabditis elegans*, and, although the situation in vertebrates is less clear[61,62], IFT-B could move into cilia after CPLANE knockdown via direct association with the homodimeric Kif17. Finally, the role for diffusion in axonemal transport is only now coming into focus[20,63], so it is at least possible that IFT-B in this case moves in the axoneme in such a manner.

Finally, our data implicate CPLANE in diverse ciliopathies. Because SRPS is generally associated with disruption of IFT-A[51,52], our identification of *INTU* mutations in patients with SRPS provides a genetic complement to our proteomic and cell biological linkage of CPLANE to IFT-A. Our identification of CPLANE gene mutations in patients with OFD similarly parallels the physical and functional association of CPLANE with Jbts17. Additional insights into the mechanism of CPLANE gene mutation in human disease will certainly emerge as we venture deeper into the CPLANE protein interaction network. For example, *WDPCP* mutations have been found in at least one patient with Bardet–Biedl syndrome[36]; thus, the links between CPLANE proteins and CCT are interesting because BBS6, BBS10 and BBS12 also interact with CCT[27,28]. Our data may also shed light on the still murky role of *FUZ* in human neural tube defects[64]. Finally, our data suggest that CPLANE may be relevant not only to congenital defects but also to infectious disease, as recent data link FUZ and the endocytic machinery to alphavirus entry[65], and we observed extensive interactions between CPLANE and the vesicle trafficking machinery (**Fig. 1b** and **Supplementary Fig. 2b**). In sum, our data establish CPLANE as a new ciliogenic protein module with important roles in development and human disease.

URLs. ProteomeXchange, http://www.proteomexchange.org/; Cytoscape, http://www.cytoscape.org/.

METHODS

Methods and any associated references are available in the online version of the paper.

Note: Any Supplementary Information and Source Data files are available in the online version of the paper.

ACKNOWLEDGMENTS

We thank the patients and their families, the IntegraGen society for exome analysis and the NHLBI GO Exome Sequencing Project, which produced and provided exome variant calls for comparison: Lung GO Sequencing Project (HL-102923), WHI Sequencing Project (HL-102924), Broad GO Sequencing Project (HL-102925), Seattle GO Sequencing Project (HL-102926) and Heart GO Sequencing Project (HL-103010). We thank the Biological Resources Center–Ferdinand Cabanne (Dijon, France) for fibroblast centralization and storage. Sequencing was provided by the University of Washington Center for Mendelian Genomics (UW CMG) and was funded by the NHGRI and NHLBI (grant 1U54 HG006493) to D. Nickerson, J. Shendure and M. Bamshad. This work was supported by grants from the following: Uehara Memorial Foundation Fellowship to M.T.; an NIDCR NRSA to J.M.T.; the French Rare Diseases Foundation, the French Ministry of Health (PHRC national 2010-A01014-35 to C.T.-R.) and the Regional Council of Burgundy to C.T.-R.; NIDDK (DK1068306) to F.H., who is a Howard Hughes Medical Institute investigator, a Doris Duke Distinguished Clinical Scientist and the Warren E. Grupe Professor; NIAMS (AR061485) to J.C.; BBSRC (BB/K010492/1) and MRC (MR/L017237/1) to K.J.L.; NIH, NSF, CPRIT and the Welch Foundation (F-1515) to E.M.M.; R01 AR066124, March of Dimes and the Joseph Drown Foundation, NIH/NCATS UCLA CTSI grant UL1TR000124 to D.K.; R01 AR062651 to D.H.C.; NIGMS (GM114276), Baxter Laboratory, the Stanford Department of Research and NIGMS (GM114276) to P.K.J.; and NIGMS (GM104853) and NHLBI (HL117164) to J.B.W., who was a Howard Hughes Medical Institute Early Career Scientist.

AUTHOR CONTRIBUTIONS

M.T. contributed to the design, execution and interpretation of the overall research plan, with special emphasis on all *Xenopus* embryo experiments and *in vitro* binding assays. M.T. also contributed to writing the manuscript. C.L. designed, performed and interpreted live imaging of IFT particles in axonemes and contributed to other imaging experiments in *Xenopus*. K.D. and E.M.M. provided protein structural models. J.M.T., J.C. and K.J.L. contributed to the design, execution and interpretation of mouse genetic data. M.R.K. contributed to the execution and analysis of the proteomic data. S.K. contributed targeted coimmunoprecipitation data that confirmed CPLANE interactions. T.J.P. contributed to *Xenopus* studies. S.P.T., I.D., D.H.C., A.-L.B., D.A.B., G.P., A.B., K.W., A.M., I.P., B.F., H.A.A., Y.Y., Y.J.C., the University of Washington Center for Mendelian Genomics, Y.D., L.F. and J.-B.R. contributed to the collection of human patient and sequencing data. F.H., C.T.-R. and D.K. contributed to the design, execution and interpretation of human genetic data. P.K.J. contributed to coordinating the overall research effort with a focus on the design and interpretation of the proteomic screen and contributed to writing the manuscript. J.B.W. coordinated the overall research effort, oversaw experimental design and interpretation, and wrote the manuscript.

COMPETING FINANCIAL INTERESTS

The authors declare no competing financial interests.

1. Hildebrandt, F., Benzing, T. & Katsanis, N. Ciliopathies. *N. Engl. J. Med.* **364**, 1533–1543 (2011).
2. Oh, E.C. & Katsanis, N. Cilia in vertebrate development and disease. *Development* **139**, 443–448 (2012).
3. Nachury, M.V. *et al.* A core complex of BBS proteins cooperates with the GTPase Rab8 to promote ciliary membrane biogenesis. *Cell* **129**, 1201–1213 (2007).
4. Sang, L. *et al.* Mapping the NPHP–JBTS–MKS protein network reveals ciliopathy disease genes and pathways. *Cell* **145**, 513–528 (2011).
5. Garcia-Gonzalo, F.R. *et al.* A transition zone complex regulates mammalian ciliogenesis and ciliary membrane composition. *Nat. Genet.* **43**, 776–784 (2011).
6. Kobayashi, D. & Takeda, H. Ciliary motility: the components and cytoplasmic preassembly mechanisms of the axonemal dyneins. *Differentiation* **83**, S23–S29 (2012).
7. Cole, D.G. *et al. Chlamydomonas* kinesin-II-dependent intraflagellar transport (IFT): IFT particles contain proteins required for ciliary assembly in *Caenorhabditis elegans* sensory neurons. *J. Cell Biol.* **141**, 993–1008 (1998).
8. Kozminski, K.G., Johnson, K.A., Forscher, P. & Rosenbaum, J.L. A motility in the eukaryotic flagellum unrelated to flagellar beating. *Proc. Natl. Acad. Sci. USA* **90**, 5519–5523 (1993).
9. Pazour, G.J., Wilkerson, C.G. & Witman, G.B. A dynein light chain is essential for the retrograde particle movement of intraflagellar transport (IFT). *J. Cell Biol.* **141**, 979–992 (1998).
10. Piperno, G. *et al.* Distinct mutants of retrograde intraflagellar transport (IFT) share similar morphological and molecular defects. *J. Cell Biol.* **143**, 1591–1601 (1998).
11. Iomini, C., Babaev-Khaimov, V., Sassaroli, M. & Piperno, G. Protein particles in *Chlamydomonas* flagella undergo a transport cycle consisting of four phases. *J. Cell Biol.* **153**, 13–24 (2001).
12. Pedersen, L.B., Geimer, S. & Rosenbaum, J.L. Dissecting the molecular mechanisms of intraflagellar transport in *chlamydomonas*. *Curr. Biol.* **16**, 450–459 (2006).
13. Rompolas, P., Pedersen, L.B., Patel-King, R.S. & King, S.M. *Chlamydomonas* FAP133 is a dynein intermediate chain associated with the retrograde intraflagellar transport motor. *J. Cell Sci.* **120**, 3653–3665 (2007).
14. Ou, G., Blacque, O.E., Snow, J.J., Leroux, M.R. & Scholey, J.M. Functional coordination of intraflagellar transport motors. *Nature* **436**, 583–587 (2005).
15. Mukhopadhyay, S. *et al.* TULP3 bridges the IFT-A complex and membrane phosphoinositides to promote trafficking of G protein–coupled receptors into primary cilia. *Genes Dev.* **24**, 2180–2193 (2010).
16. Liem, K.F. Jr. *et al.* The IFT-A complex regulates Shh signaling through cilia structure and membrane protein trafficking. *J. Cell Biol.* **197**, 789–800 (2012).
17. Behal, R.H. *et al.* Subunit interactions and organization of the *Chlamydomonas reinhardtii* intraflagellar transport complex A proteins. *J. Biol. Chem.* **287**, 11689–11703 (2012).

18. Lucker, B.F. *et al.* Characterization of the intraflagellar transport complex B core: direct interaction of the IFT81 and IFT74/72 subunits. *J. Biol. Chem.* **280**, 27688–27696 (2005).
19. Taschner, M., Bhogaraju, S. & Lorentzen, E. Architecture and function of IFT complex proteins in ciliogenesis. *Differentiation* **83**, S12–S22 (2012).
20. Craft, J.M., Harris, J.A., Hyman, S., Kner, P. & Lechtreck, K.F. Tubulin transport by IFT is upregulated during ciliary growth by a cilium-autonomous mechanism. *J. Cell Biol.* **208**, 223–237 (2015).
21. Bhogaraju, S. *et al.* Molecular basis of tubulin transport within the cilium by IFT74 and IFT81. *Science* **341**, 1009–1012 (2013).
22. Tarkar, A. *et al.* DYX1C1 is required for axonemal dynein assembly and ciliary motility. *Nat. Genet.* **45**, 995–1003 (2013).
23. Omran, H. *et al.* Ktu/PF13 is required for cytoplasmic pre-assembly of axonemal dyneins. *Nature* **456**, 611–616 (2008).
24. Mitchison, H.M. *et al.* Mutations in axonemal dynein assembly factor *DNAAF3* cause primary ciliary dyskinesia. *Nat. Genet.* **44**, 381–389, S1–S2 (2012).
25. Horani, A. *et al.* Whole-exome capture and sequencing identifies *HEATR2* mutation as a cause of primary ciliary dyskinesia. *Am. J. Hum. Genet.* **91**, 685–693 (2012).
26. Diggle, C.P. *et al.* HEATR2 plays a conserved role in assembly of the ciliary motile apparatus. *PLoS Genet.* **10**, e1004577 (2014).
27. Seo, S. *et al.* BBS6, BBS10, and BBS12 form a complex with CCT/TRiC family chaperonins and mediate BBSome assembly. *Proc. Natl. Acad. Sci. USA* **107**, 1488–1493 (2010).
28. Zhang, Q., Yu, D., Seo, S., Stone, E.M. & Sheffield, V.C. Intrinsic protein–protein interaction-mediated and chaperonin-assisted sequential assembly of stable Bardet–Biedl syndrome protein complex, the BBSome. *J. Biol. Chem.* **287**, 20625–20635 (2012).
29. Goetz, S.C., Liem, K.F. Jr. & Anderson, K.V. The spinocerebellar ataxia-associated gene Tau tubulin kinase 2 controls the initiation of ciliogenesis. *Cell* **151**, 847–858 (2012).
30. Ye, X., Zeng, H., Ning, G., Reiter, J.F. & Liu, A. C2cd3 is critical for centriolar distal appendage assembly and ciliary vesicle docking in mammals. *Proc. Natl. Acad. Sci. USA* **111**, 2164–2169 (2014).
31. Singla, V., Romaguera-Ros, M., Garcia-Verdugo, J.M. & Reiter, J.F. *Ofd1*, a human disease gene, regulates the length and distal structure of centrioles. *Dev. Cell* **18**, 410–424 (2010).
32. Joo, K. *et al.* CCDC41 is required for ciliary vesicle docking to the mother centriole. *Proc. Natl. Acad. Sci. USA* **110**, 5987–5992 (2013).
33. Adler, P.N., Charlton, J. & Park, W.J. The *Drosophila* tissue polarity gene *inturned* functions prior to wing hair morphogenesis in the regulation of hair polarity and number. *Genetics* **137**, 829–836 (1994).
34. Collier, S. & Gubb, D. *Drosophila* tissue polarity requires the cell-autonomous activity of the *fuzzy* gene, which encodes a novel transmembrane protein. *Development* **124**, 4029–4037 (1997).
35. Collier, S., Lee, H., Burgess, R. & Adler, P. The WD40 repeat protein fritz links cytoskeletal planar polarity to frizzled subcellular localization in the *Drosophila* epidermis. *Genetics* **169**, 2035–2045 (2005).
36. Kim, S.K. *et al.* Planar cell polarity acts through septins to control collective cell movement and ciliogenesis. *Science* **329**, 1337–1340 (2010).
37. Park, T.J., Haigo, S.L. & Wallingford, J.B. Ciliogenesis defects in embryos lacking inturned or fuzzy function are associated with failure of planar cell polarity and Hedgehog signaling. *Nat. Genet.* **38**, 303–311 (2006).
38. Huttlin, E.L. *et al.* The BioPlex network: a systematic exploration of the human interactome. *Cell* **162**, 425–440 (2015).
39. Rual, J.F. *et al.* Towards a proteome-scale map of the human protein–protein interaction network. *Nature* **437**, 1173–1178 (2005).
40. Wang, Y., Yan, J., Lee, H., Lu, Q. & Adler, P.N. The proteins encoded by the *Drosophila* planar polarity effector genes *inturned*, *fuzzy* and *fritz* interact physically and can re-pattern the accumulation of "upstream" planar cell polarity proteins. *Dev. Biol.* **394**, 156–169 (2014).
41. Gray, R.S. *et al.* The planar cell polarity effector Fuz is essential for targeted membrane trafficking, ciliogenesis and mouse embryonic development. *Nat. Cell Biol.* **11**, 1225–1232 (2009).
42. Alazami, A.M. *et al.* Molecular characterization of Joubert syndrome in Saudi Arabia. *Hum. Mutat.* **33**, 1423–1428 (2012).
43. Lopez, E. *et al. C5orf42* is the major gene responsible for OFD syndrome type VI. *Hum. Genet.* **133**, 367–377 (2014).
44. Shaheen, R. *et al.* Genomic analysis of Meckel–Gruber syndrome in Arabs reveals marked genetic heterogeneity and novel candidate genes. *Eur. J. Hum. Genet.* **21**, 762–768 (2013).
45. Srour, M. *et al.* Mutations in *C5orf42* cause Joubert syndrome in the French Canadian population. *Am. J. Hum. Genet.* **90**, 693–700 (2012).
46. Damerla, R.R. *et al.* Novel *Jbts17* mutant mouse model of Joubert syndrome with cilia transition zone defects and cerebellar and other ciliopathy related anomalies. *Hum. Mol. Genet.* **24**, 3994–4005 (2015).
47. Brooks, E.R. & Wallingford, J.B. Control of vertebrate intraflagellar transport by the planar cell polarity effector Fuz. *J. Cell Biol.* **198**, 37–45 (2012).
48. Brooks, E.R. & Wallingford, J.B. The small GTPase Rsg1 is important for the cytoplasmic localization and axonemal dynamics of intraflagellar transport proteins. *Cilia* **2**, 13 (2013).
49. Gurrieri, F., Franco, B., Toriello, H. & Neri, G. Oral-facial-digital syndromes: review and diagnostic guidelines. *Am. J. Med. Genet. A.* **143A**, 3314–3323 (2007).
50. Tabler, J.M. *et al. Fuz* mutant mice reveal shared mechanisms between ciliopathies and FGF-related syndromes. *Dev. Cell* **25**, 623–635 (2013).
51. Merrill, A.E. *et al.* Ciliary abnormalities due to defects in the retrograde transport protein DYNC2H1 in short-rib polydactyly syndrome. *Am. J. Hum. Genet.* **84**, 542–549 (2009).
52. Mill, P. *et al.* Human and mouse mutations in *WDR35* cause short-rib polydactyly syndromes due to abnormal ciliogenesis. *Am. J. Hum. Genet.* **88**, 508–515 (2011).
53. Hsieh, Y.C. & Hou, J.W. Oral-facial-digital syndrome with Y-shaped fourth metacarpals and endocardial cushion defect. *Am. J. Med. Genet.* **86**, 278–281 (1999).
54. Panigrahi, I., Das, R.R., Kulkarni, K.P. & Marwaha, R.K. Overlapping phenotypes in OFD type II and OFD type VI: report of two cases. *Clin. Dysmorphol.* **22**, 109–114 (2013).
55. Saari, J., Lovell, M.A., Yu, H.C. & Bellus, G.A. Compound heterozygosity for a frame shift mutation and a likely pathogenic sequence variant in the planar cell polarity–ciliogenesis gene *WDPCP* in a girl with polysyndactyly, coarctation of the aorta, and tongue hamartomas. *Am. J. Med. Genet. A.* **167A**, 421–427 (2015).
56. Li, Y. *et al.* Global genetic analysis in mice unveils central role for cilia in congenital heart disease. *Nature* **521**, 520–524 (2015).
57. Cui, C. *et al.* Wdpcp, a PCP protein required for ciliogenesis, regulates directional cell migration and cell polarity by direct modulation of the actin cytoskeleton. *PLoS Biol.* **11**, e1001720 (2013).
58. Butler, M.T. & Wallingford, J.B. Control of vertebrate core planar cell polarity protein localization and dynamics by Prickle 2. *Development* **142**, 3429–3439 (2015).
59. Zilber, Y. *et al.* The PCP effector Fuzzy controls cilial assembly and signaling by recruiting Rab8 and Dishevelled to the primary cilium. *Mol. Biol. Cell* **24**, 555–565 (2013).
60. van Dam, T.J. *et al.* Evolution of modular intraflagellar transport from a coatomer-like progenitor. *Proc. Natl. Acad. Sci. USA* **110**, 6943–6948 (2013).
61. Pan, X. *et al.* Mechanism of transport of IFT particles in *C. elegans* cilia by the concerted action of kinesin-II and OSM-3 motors. *J. Cell Biol.* **174**, 1035–1045 (2006).
62. Snow, J.J. *et al.* Two anterograde intraflagellar transport motors cooperate to build sensory cilia on *C. elegans* neurons. *Nat. Cell Biol.* **6**, 1109–1113 (2004).
63. Harris, J.A., Liu, Y., Yang, P., Kner, P. & Lechtreck, K.F. Single particle imaging reveals IFT-independent transport and accumulation of EB1 in *Chlamydomonas* flagella. *Mol. Biol. Cell* **27**, 295–307 (2016).
64. Seo, J.H. *et al.* Mutations in the planar cell polarity gene, Fuzzy, are associated with neural tube defects in humans. *Hum. Mol. Genet.* **20**, 4324–4333 (2011).
65. Ooi, Y.S., Stiles, K.M., Liu, C.Y., Taylor, G.M. & Kielian, M. Genome-wide RNAi screen identifies novel host proteins required for alphavirus entry. *PLoS Pathog.* **9**, e1003835 (2013).

ONLINE METHODS

Study overview. The methods used in this study were essentially those described previously. Immunoprecipitation of LAP-tagged CPLANE proteins was performed as described[4]. General methods for experiments with *Xenopus* were performed as described[36,37]. Imaging of IFT proteins at basal bodies and time-lapse imaging of IFT were performed as described[47]. Exome sequencing was performed essentially as described[4,43].

Tandem affinity purification and mass spectrometry. To best optimize the LAP purification procedure and minimize the possibility of carryover, we standardized the growth of cells, the preparation of extracts and the method of tandem affinity purification. Briefly, cell lines with stable expression of LAP-tagged proteins were collected using detergent. The mouse IMCD3 renal cell line was obtained from the American Type Culture Collection (CRL-2123). The cell line was authenticated by examining the expression of renal markers (AQP2), polarization, establishment of tight junctions and ciliation, as outlined in ref. 66. Cells tested negative for mycoplasma contaminaiton. Lysates were clarified by centrifugation at 280,000*g* and subjected to immunoprecipitation with an affinity-purified rabbit antibody to GFP produced in house. Bound proteins were eluted from antibody-conjugated beads using TEV protease, recaptured on S-protein agarose (Novagen) and eluted in 4× NuPAGE sample buffer (Invitrogen). Following purification, great care was taken to ensure a lack of contamination from both environmental sources and other purified proteins. Each purified set of interacting proteins was separated on an individual 10% Bis-Tris polyacrylamide gel and stained with Coomassie Brilliant Blue. IMCD3 samples were run on gels for 20–40 mm and divided into 20- to 40-mm × 1-mm slices. Each excised lane was reduced, carboxyamidomethylated and digested with trypsin. Peptide identification of each digestion mixture was performed by microcapillary reverse-phase HPLC nanoelectrospray tandem mass spectrometry (mLC-MS/MS) on an LTQ-Orbitrap Velos or XL mass spectrometer (Thermo Fisher Scientific). The Orbitrap repetitively surveyed a mass/charge (m/z) range from 395 to 1,600, while data-dependent MS/MS spectra on the 20 (Velos) or 10 (XL) most abundant ions in each survey scan were acquired in the linear ion trap. MS/MS spectra were acquired with a relative collision energy of 30%, an isolation width of 2.5 Da and dynamic exclusion of recurring ions for 60 s. Preliminary sequencing of peptides was facilitated with the SEQUEST algorithm with a mass tolerance of 30 ppm against a species-specific (mouse or human) subset of the UniProt Knowledgebase. With a custom version of the Harvard Proteomics Browser Suite (Thermo Fisher Scientific), peptide spectrum matches (PSMs) were accepted with mass error <2.5 ppm and score thresholds to attain an estimated false discovery rate (FDR) of <1% using a reverse-decoy database strategy. For IMCD3 LAP-GFP control samples, peptide identification was performed using NanoAcquity UPLC (Waters Corp.). Samples were analyzed on-line via nanospray ionization into a hybrid LTQ-Orbitrap mass spectrometer (Thermo Scientific). Data were collected in data-dependent mode with the parent ion analyzed in the FTMS and the top eight most abundant ions selected for fragmentation and analysis in the LTQ. Tandem mass spectrometry data were analyzed using the Mascot search algorithm (Matrix Sciences) against the mouse UniProt database (including reverse hits and contaminants) and filtered to a 5% FDR.

Tandem affinity purification and network generation with mass spectrometry data. For individual genes identified in each affinity purification/MS sample, we calculated the normalized spectral abundance factor (NSAF)

$$\mathrm{NSAF} = \frac{P_g / L_g}{\sum_i P_i / L_i}$$

where P_g represents the number of spectral counts mapped to gene g and L_g is the mean length, in residues, of reference protein isoforms derived from that gene. The P/L quotient is normalized to the sum of the P/L quotients for all genes in the data set, excluding those derived from the bait protein and those derived from known exogenous proteins. We excluded, for example, proteins commonly found in skin and enzymes added during sample preparation. Using an unpublished set of eight negative-control data sets, we systematically searched for genes whose score in an experimental data set was highly unlikely. These filtered genes are provided as a Cytoscape network file (**Supplementary Data 2**); a manually curated, simplified subset of these is shown in **Figure 1b**.

***Xenopus* embryo manipulations and microinjections.** Female adult *Xenopus* were induced to ovulation by injection with human chorionic gonadotropin, and eggs were fertilized *in vitro*, dejellied in 3% cysteine (pH 7.9) at the two-cell stage and subsequently reared in 0.3× Marc's modified Ringer's (MMR) solution. For microinjections, embryos were placed in a solution of 2% Ficoll in 0.3× MMR and handled using forceps and an Oxford universal micromanipulator. After injections, embryos were reared for 3 h in 2% Ficoll in 0.3× MMR and then washed and reared in 0.3× MMR until the appropriate stages were reached. All experiments were repeated in multiple embryos from multiple clutches, as is standard in the field. No explicit randomization or blinding strategy was employed. Sex cannot be practically determined for the tadpoles used in these studies. This work was carried out with the approval of the University of Texas Animal Care and Use Committee.

Morpholinos, mRNA and genomic RNA injections. Capped mRNA was synthesized using an mMESSAGE mMACHINE kit (Ambion). mRNA and antisense MOs were injected into two ventral blastomeres or two dorsal blastomeres at the four-cell stage to target the epidermis and neural tissues, respectively[67]. MO sequences and working concentrations are provided in **Supplementary Table 3**.

We note that the *intu*, *fuz* and *wdpcp* MOs used here elicit phenotypes validated by genetic disruption of the corresponding genes in mice[36,37,57,68]. The *rsg1* MO has been validated by disruption of the Rsg1 GTPase by expression of a dominant-negative mutant[41].

Plasmid constructs. Three cDNA fragments encoding *Xenopus* Jbts17 were amplified by PCR from a stage 25 *Xenopus* cDNA library with the primers listed in **Supplementary Table 3**. These three PCR products were then fused to generate full-length cDNA by PCR with SmaI and NotI restriction enzyme sites at 5′ and 3′ ends, respectively. Truncated mutants were generated by PCR. The cDNAs were then subcloned into various pCS107 vectors that established fusion with an EGFP, mRFP or Myc tag at the N terminus of the encoded protein.

Full-length *ofd1*, *cep164*, *hook2*, *mks1*, *ift122*, *ift140*, *ift144*, *ift43*, *ift121*, *ift139*, *ift81*, *ift80* and *cluap1* cDNAs were identified in Xenbase[69], amplified by PCR and subcloned into pCS107 vectors to encode proteins fused with GFP, RFP or mCherry at their N termini. Rsg1, Ift20, Ift43, Cetn4 and Intu constructs were previously described[47,48,70]. GFP-tagged CFAP20 was kindly gifted by B. Mitchell (Northwestern University).

***In vitro* protein translation and pulldown assays.** GFP-tagged Intu, Fuz and Wdpcp and FLAG-tagged Jbts17 (amino acids 907–1569) were synthesized using a TNT SP6 Coupled Wheat Germ Extract System (Promega). After centrifugation at 17,000*g* at 4 °C for 10 min, the synthesized soluble proteins were mixed and incubated in binding buffer (20 mM Tris-HCl, pH 8.0, 1 mM EDTA, 1 mM DTT and 150 mM NaCl) for 2 h at 4 °C. FLAG-tagged Jbts17 protein was precipitated with anti-FLAG M2 magnetic beads (Sigma-Aldrich). The beads were washed with binding buffer containing 0.1% Triton X-100 four times and eluted with 200 ng/ml FLAG peptide in 1× TBS. The eluted proteins were analyzed by immunoblotting with antibody to GFP (Abcam) and anti-FLAG M2 antibody (Sigma-Aldrich) (1:2,000 dilution).

sgRNA synthesis, CRISPR/Cas9-induced genomic editing and genotyping. CRISPR/Cas9-mediated genome editing in *Xenopus* was performed as previously described[71]. Briefly, the amplicon was purified by PCR purification kit (Qiagen) and used as a template for single guide RNA (sgRNA) synthesis. sgRNA was generated using the T7 MEGAscript kit (Ambion) and purified by MEGAclear Transcription Cleanup kit (Ambion). 1.25 ng of Cas9 protein (PNABIO) and 250 pg of sgRNA were injected into the animal pole at the one-cell stage. Genomic DNA was extracted from stage 25 embryos using the DNeasy Blood and Tissue kit (Qiagen) following the manufacturer's protocol, and the 46-bp genomic region that contained the sgRNA target sequence was amplified by PCR. The efficiency of CRISPR/Cas9-mediated genome editing

was examined by T7 endonuclease I (T7EI) assay and NcoI digestion, with fragments analyzed by 2% agarose gel.

Basal body imaging and quantification. Fluorescence images of GFP, RFP or BFP fusion proteins at basal bodies in stage 25–28 MCCs were captured with an LSM700 inverted confocal microscope (Carl Zeiss) with a Plan-APOCHROMAT 63×/1.4 NA oil-immersion objective. The fluorescence intensities of GFP, RFP or BFP fusion proteins at basal bodies in 2-mm slices of apical surface were measured by the three-dimensional object counter plugin of Fiji software as described previously[47,48]. The object size was set to 20, and the threshold was determined empirically to maximize detection of apparent foci. At least 14 basal bodies per cell from at least 12 cells in four independent embryos were analyzed. Statistical analysis was subsequently performed, making use of Student's *t* test.

Live imaging of IFT particles and analysis. For high-speed *in vivo* imaging, *Xenopus* embryos injected with mRNAs encoding GFP-tagged IFT proteins and membrane-RFP were anaesthetized with 0.005% benzocaine at stages 25–28. Images were acquired on a Nikon Eclipse Ti confocal microscope with a 63×/1.4 NA oil-immersion objective. Time-lapse series were captured at 266.5 ms/frame. Kymographs were generated and IFT velocities were measured in Fiji with the kymograph plugin.

Super-resolution microscopy. GFP-Jbts17, mCherry-Cep164 and Cetn4-BFP were coexpressed by mRNA injection of epidermis in stage 27 *Xenopus* embryos. Fluorescence signals were captured on an LSM710/Elyra S.1 microscope (Carl Zeiss) via a 63×/1.3 NA oil-immersion objective. Raw fluorescence images were processed by structured illumination algorithm using Zen software (Carl Zeiss). The arbitrary units of fluorescence intensity for the ring-shaped structures of GFP-Jbts17 and mCherry-Cep164 at basal bodies were measured using the Plot Profile plugin in Fiji software.

Immunostaining. Immunostaining was performed as described[72]. Embryos were fixed in MEMFA for 2 h at room temperature after removing the vitelline envelop and washing with PBST (1× PBS containing 0.05% Triton X-100). Transverse sections of neural tube were generated from stage 22 embryos using a Vibratome series 1000, and the gastrocoel roof plate (GRP) region was manually dissected form stage 17 embryos using forceps. Sections were completely dehydrated in methanol at −20 °C overnight. After rehydration, sections were blocked with 10% FBS in PBST for 60 min and incubated with antibody to acetylated α-tubulin (1:2,000 dilution; clone 6-11B-1, Sigma) diluted in blocking solution. Primary antibody was detected with Alexa Fluor 488–conjugated goat anti-mouse IgG (Invitrogen). Fluorescence images were obtained using a Zeiss LSM700 confocal microscope. Cilia length in the neural tube and GRP was measured in Fiji software.

***In situ* hybridization.** Whole-mount *in situ* hybridization of *Xenopus* embryos was performed as described previously[73] using digoxigenin-labeled RNA probes against *nkx2.2*, *vax1* and *pitx2c*. Bright-field images were captured on a Zeiss Axiozoom V16 stereomicroscope.

RT–PCR. *jbts17* MO was injected into all cells at the four-cell stage, and total RNA was isolated using TRIzol reagent (Invitrogen) from four stage 25 *Xenopus* embryos. The stage 25 cDNA library was synthesized using M-MLV reverse transcriptase (Invitrogen) with random hexamers. *jbts17* and an ornithine decarboxylase 1 (*odc1*) internal control were amplified using Phusion High-Fidelity DNA polymerase (New England BioLabs) with the primers listed in **Supplementary Table 3**. The abundance of the resulting amplicon was analyzed on a 2% agarose gel stained with ethidium bromide under a UV transilluminator.

Protein structure modeling. For fold recognition studies of Fuz, Intu, Wdpcp, Jbts17 and Rsg1, we used HHpred[74] and pGenThreader[75] with default parameters searched against the latest set of Protein Data Bank (PDB) structures. We used the respective Modeller pipelines on the HHpred and pGenThreader servers to build homology models based on high-confidence fold recognition results. The validity of the homology models was checked using automated scores provided by HHpred. Additionally, DaliLite[76] was used to align the homology models with the original template for visual inspection of the fold.

Human subjects. The committees approving work with human subjects included GAD collection DC2011-1332 (C.T.-R.), the institutional review boards of the University of Michigan and Boston Children's Hospital (F.H.), and the Human Subjects Institutional Review Board of the University of California, Los Angeles (D.K.). Informed consent was obtained from all study participants, and consent was obtained for use of all images of human subjects.

66. Giles, R.H., Ajzenberg, H. & Jackson, P.K. 3D spheroid model of mIMCD3 cells for studying ciliopathies and renal epithelial disorders. *Nat. Protoc.* **9**, 2725–2731 (2014).
67. Moody, S.A. & Kline, M.J. Segregation of fate during cleavage of frog (*Xenopus laevis*) blastomeres. *Anat. Embryol. (Berl.)* **182**, 347–362 (1990).
68. Zeng, H., Hoover, A.N. & Liu, A. PCP effector gene *Inturned* is an important regulator of cilia formation and embryonic development in mammals. *Dev. Biol.* **339**, 418–428 (2010).
69. Karpinka, J.B. *et al.* Xenbase, the *Xenopus* model organism database; new virtualized system, data types and genomes. *Nucleic Acids Res.* **43**, D756–D763 (2015).
70. Park, T.J., Mitchell, B.J., Abitua, P.B., Kintner, C. & Wallingford, J.B. Dishevelled controls apical docking and planar polarization of basal bodies in ciliated epithelial cells. *Nat. Genet.* **40**, 871–879 (2008).
71. Nakayama, T. *et al.* Cas9-based genome editing in *Xenopus tropicalis*. *Methods Enzymol.* **546**, 355–375 (2014).
72. Lee, C., Kieserman, E., Gray, R.S., Park, T.J. & Wallingford, J. Whole-mount fluorescence immunocytochemistry on *Xenopus* embryos. *CSH Protoc.* **2008**, pdb.prot4957 (2008).
73. Sive, H.L., Grainger, R.M. & Harland, R.M. *Early Development of Xenopus* laevis: *A Laboratory Manual* (Cold Spring Harbor Press, 2000).
74. Söding, J. Protein homology detection by HMM-HMM comparison. *Bioinformatics* **21**, 951–960 (2005).
75. Lobley, A., Sadowski, M.I. & Jones, D.T. pGenTHREADER and pDomTHREADER: new methods for improved protein fold recognition and superfamily discrimination. *Bioinformatics* **25**, 1761–1767 (2009).
76. Hasegawa, H. & Holm, L. Advances and pitfalls of protein structural alignment. *Curr. Opin. Struct. Biol.* **19**, 341–348 (2009).

doi:10.1038/ng.3558

Corrigendum: The ciliopathy-associated CPLANE proteins direct basal body recruitment of intraflagellar transport machinery

Michinori Toriyama, Chanjae Lee, S Paige Taylor, Ivan Duran, Daniel H Cohn, Ange-Line Bruel, Jacqueline M Tabler, Kevin Drew, Marcus R Kelly, Sukyoung Kim, Tae Joo Park, Daniela A Braun, Ghislaine Pierquin, Armand Biver, Kerstin Wagner, Anne Malfroot, Inusha Panigrahi, Brunella Franco, Hadeel Adel Al-lami, Yvonne Yeung, Yeon Ja Choi, University of Washington Center for Mendelian Genomics, Yannis Duffourd, Laurence Faivre, Jean-Baptiste Rivière, Jiang Chen, Karen J Liu, Edward M Marcotte, Friedhelm Hildebrandt, Christel Thauvin-Robinet, Deborah Krakow, Peter K Jackson & John B Wallingford
***Nat. Genet.* 48, 648–656 (2016); published online 9 May 2016; corrected after print 30 May 2016**

In the version of this article initially published, the name of author Daniela A. Braun was misspelled. The error has been corrected in the HTML and PDF versions of the article.